Journal of Nuclear Materials 451 (2014) 372–378

Contents lists available at ScienceDirect

Journal of Nuclear Materials

journal homepage: www.elsevier.com/locate/jnucmat

Effects of Cr and Ni on interdiffusion and reaction between U and Fe–Cr–Ni alloys

K. Huang [a], Y. Park [a], L. Zhou [a], K.R. Coffey [a], Y.H. Sohn [a,*], B.H. Sencer [b], J.R. Kennedy [b]

[a] *Advanced Materials Processing and Analysis Center, Department of Materials Science and Engineering, University of Central Florida, Orlando, FL, USA*
[b] *Fundamental Fuel Properties Department, Nuclear Fuel and Materials Division Idaho National Laboratory, Idaho Falls, ID, USA*

ARTICLE INFO

Article history:
Received 20 November 2013
Accepted 7 April 2014
Available online 13 April 2014

ABSTRACT

Metallic U-alloy fuel cladded in steel has been examined for high temperature fast reactor technology wherein the fuel cladding chemical interaction is a challenge that requires a fundamental and quantitative understanding. In order to study the fundamental diffusional interactions between U with Fe and the alloying effect of Cr and Ni, solid-to-solid diffusion couples were assembled between pure U and Fe, Fe–15 wt.%Cr or Fe–15 wt.%Cr–15 wt.%Ni alloy, and annealed at high temperature ranging from 580 to 700 °C. The microstructures and concentration profiles that developed from the diffusion anneal were examined by scanning electron microscopy, and X-ray energy dispersive spectroscopy (XEDS), respectively. Thick U_6Fe and thin UFe_2 phases were observed to develop with solubilities: up to 2.5 at.% Ni in $U_6(Fe,Ni)$, up to 20 at.%Cr in $U(Fe, Cr)_2$, and up to 7 at.%Cr and 14 at.% Ni in $U(Fe, Cr, Ni)_2$. The interdiffusion and reactions in the U vs. Fe and U vs. Fe–Cr–Ni exhibited a similar temperature dependence, while the U vs. Fe–Cr diffusion couples, without the presence of Ni, yielded greater activation energy for the growth of intermetallic phases – lower growth rate at lower temperature but higher growth rate at higher temperature.

1. Introduction

Uranium–zirconium (U–Zr) metallic fuel with stainless steel cladding has been in development for advanced fast reactors because of its high burn-up capability and favorable thermal response [1–3]. Under irradiation, the U–Zr fuel can swell and make contact with the stainless steel cladding because of thermal expansion and the accumulation of fission products, resulting in interdiffusion and formation of new phases. This fuel cladding chemical interaction (FCCI) can have deleterious effects, because it can thin the cladding and produce phases with undesirable properties. The FCCI between U–Zr alloys and stainless steels, including U–Zr vs. Fe [4–6], U–Zr vs. Fe–Cr [4,6], U–Zr vs. Fe–Ni [4], U–Zr vs. Fe–Cr–Ni [4] and U–Zr vs. steel (e.g., D9, 316, HT9) [7–9], has been a subject of many previous investigations. Typically, the interaction zone that develops due to interdiffusion and reaction consists of a complex multi-layer structure with various intermetallic compounds. Due to the complexities, these studies, in general, lacked quantitative kinetic results and suffered experimental discrepancies associated with poor resolution for the complex microstructural features. In order to help understand the complex FCCI process, we have carried out a systematic experimental investigation in U–Zr vs. Fe–Cr–Ni alloys. This paper reports the interdiffusion and reaction between U and Fe–Cr–Ni alloys. The effects of the alloying elements, Cr and Ni, are emphasized, based on our previous quantitative study [10] of interdiffusion and reaction between pure U and pure Fe.

In our previous study [10], the reactions between pure U and pure Fe were investigated in the temperature range from 580 to 700 °C to form a baseline for the comprehensive investigation on the U–Zr–Fe–Ni–Cr system. The U_6Fe (*tI28*, *I4/mcm*) and UFe_2 (*cF24*, $Fd\bar{3}m$) intermetallic phases developed in all diffusion couples [10], consistent with the equilibrium phase diagram of U–Fe shown in Fig. 1 [11]. The integrated interdiffusion flux, intrinsic and extrinsic growth constants of both phases were determined. The effect of allotropic transformation of U on the reaction and reaction mechanism between U and Fe was also discussed. For the sake of clarity and continuity, results from our previous

---

[*] Corresponding author. Address: Department of Materials Science and Engineering, 12760 Pegasus Drive, Engineering 1 (Bldg 40), Room 211, University of Central Florida, Orlando, FL 32816, United States. Address: Materials Characterization Facility (MCF), Advanced Materials Processing and Analysis Center (AMPAC), 12443 Research Parkway, Suite 302, University of Central Florida, Orlando, FL 32816, United States. Tel.: +1 407 882 1181 (AMPAC), +1 407 823 1838 (MSE), +1 407 882 1500 (MCF); fax: +1 407 882 1461.

E-mail address: Yongho.Sohn@ucf.edu (Y.H. Sohn).

http://dx.doi.org/10.1016/j.jnucmat.2014.04.009
0022-3115/

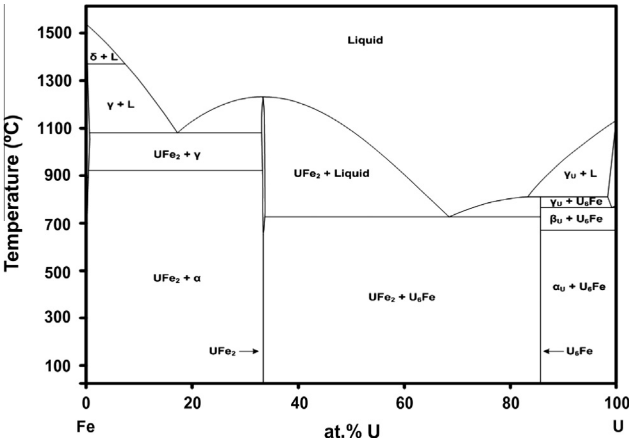

Fig. 1. Equilibrium binary phase diagram of U–Fe system [11].

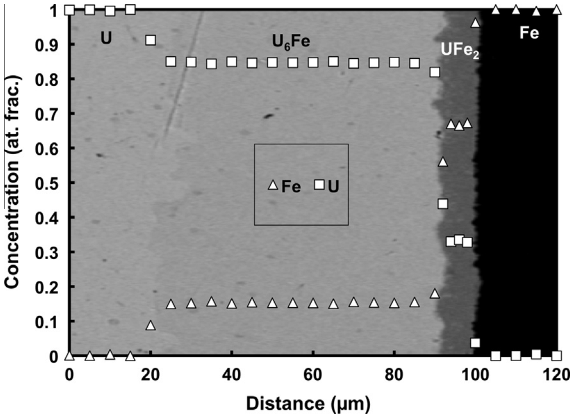

Fig. 2. Backscattered electron micrograph and concentration profiles obtained from the U vs. Fe diffusion couple annealed at 650 °C for 96 h.

study on pure U vs. pure Fe are briefly highlighted as a part of this paper.

In order to examine the effects of Cr and Ni alloying additions, solid-to-solid diffusion experiments were carried out for U vs. Fe–15 wt.%Cr and U vs. Fe–15 wt.%Cr–15 wt.%Ni couples, annealed at 600, 650 and 700 °C for 240, 96 and 96 h, respectively. Scanning electron microscopy (SEM) and X-ray energy dispersive spectroscopy (XEDS) were employed to examine the development of intermetallic phases in the interdiffusion zone. Semi-quantitative standard-less XEDS analyses were employed to determine the concentration profiles and relevant thermo-kinetic coefficients.

2. Experimental procedure

All metallographical preparation and assembly of diffusion couples were carried out under an argon (Ar) atmosphere inside a glove box to minimize oxidation of the depleted U (DU), Fe, Fe–Cr and Fe–Cr–Ni alloys. DU rods were cast using high-purity depleted uranium (DU) via arc melting. They were melted three times to ensure homogeneity, and then drop-cast to form rods with 12.7 mm diameter. Pure Fe, also in the form of rod with similar diameter, was acquired from a commercial source (Alpha-Aesar™), while Fe–15 wt.%Cr and Fe–15 wt.%Cr–15 wt.%Ni alloys were produced using a similar arc melting process as described for the DU rods. All metals and alloys employed in this study had a grain size in the range of tens to hundreds of micrometers.

Both the DU and Fe alloy rods were sectioned into 3 mm thick discs and the surfaces were metallographically polished down to a 1 μm roughness using diamond paste. Immediately before the assembly of the diffusion couples, the DU discs were immersed momentarily into nitric acid (1:1 volume with distilled water) to remove the surface oxide layer. The prepared alloy disks were assembled together to form diffusion couples and sealed into a quartz capsule under vacuum (10^{-6} Pa). After annealing in a Lindberg/Blue™ three-zone tube furnace, the diffusion couples were quenched by breaking the quartz capsule in cold water. Each diffusion couple was then cross-sectioned for microstructural examination and compositional analysis. The temperature and time of the diffusion anneal are listed in Table 1 for our previous [10] and current studies. SEM and XEDS were performed to examine the interdiffusion microstructure and concentration profiles. The thickness of the intermetallic phases that developed was measured at a minimum of 10 randomly chosen locations using backscattered electron (BSE) micrographs.

Table 1
Temperature and time of anneal for the U vs. Fe [10], U vs. Fe–15 wt.%Cr and U vs. Fe–15 wt.%Cr–15 wt.%Ni diffusion couples.

Diffusion couples	Temperature (°C)	Time (h)
U vs. Fe [10]	580	240
	615	240
	650	96
	680	96
	700	96
U vs. Fe–15 wt.%Cr	600	240
	650	96
	700	96
U vs. Fe–15 wt.%Cr–15 wt.%Ni	600	240
	650	96
	700	96

3. Development of interdiffusion microstructure and concentration profiles

3.1. Brief summary of results from U vs. Fe diffusion couple study [10]

Typical backscattered electron (BSE) micrograph and concentration profiles obtained from the U vs. Fe diffusion couple annealed at 650 °C for 96 h are presented in Fig. 2. Similar microstructures were observed for couples annealed at other temperatures. The four phases shown in Fig. 2 are pure U, U_6Fe, UFe_2 and pure Fe in accordance with the U–Fe equilibrium phase diagram in Fig. 1

Table 2
Thickness of U_6Fe and UFe_2 phases developed in the U vs. Fe [10], U vs. Fe–15 wt.%Cr and U vs. Fe–15 wt.%Cr–15 wt.%Ni diffusion couples. Note that with the alloying addition of Cr and Cr–Ni in Fe–15 wt.%Cr and Fe–15 wt.%Cr–15 wt.%Ni alloys, respectively, results in the formation of UFe_2 and U_6Fe with variation in solubilities for Cr and Ni.

Diffusion couple	T (°C)	Time (h)	$\Delta x^{(U_6Fe)}$(μm)	$\Delta x^{(UFe_2)}$(μm)	Ratio $\frac{\Delta x^{(U_6Fe)}}{\Delta x^{(UFe_2)}}$
U vs. Fe [10]	580	240	46.4 ± 0.9	2.5 ± 0.1	18.6
	615	240	70.1 ± 0.8	6.0 ± 0.4	11.7
	650	96	64.1 ± 2.5	7.8 ± 0.6	8.2
	680	96	78.4 ± 2.0	8.4 ± 0.3	9.3
	700	96	90.3 ± 2.1	12.1 ± 0.5	7.5
U vs. Fe–15 wt.%Cr	600	240	40.2 ± 0.7	3.6 ± 0.2	11.2
	650	96	51.7 ± 1.1	6.1 ± 0.4	8.5
	700	96	120.5 ± 1.4	22.2 ± 1.5	5.4
U vs. Fe–15 wt.%Cr –15 wt.%Ni	600	240	54.2 ± 0.8	3.8 ± 0.3	14.3
	650	96	56.5 ± 1.3	5.6 ± 0.6	10.1
	700	96	84.4 ± 1.4	11.1 ± 0.8	7.6

Table 3

Parabolic growth rate constants, k_p of U_6Fe and UFe_2 phases along with the total interaction zone determined from the U vs. Fe [10], U vs. Fe–15 wt.%Cr and U vs. Fe–15 wt.%Cr–15 wt.%Ni diffusion couples. Note that with the alloying addition of Cr and Cr–Ni in Fe–15 wt.%Cr and Fe–15 wt.%Cr–15 wt.%Ni alloys, respectively, results in the formation of UFe_2 and U_6Fe with variation in solubilities for Cr and Ni.

Diffusion couple	T (°C)	$k_p^{U_6Fe} \times 10^{16}$ (m^2/s)	$Q_{k_p}^{U_6Fe}$ (kJ/mol)	$k_p^{UFe_2} \times 10^{15}$ (m^2/s)	$Q_{k_p}^{UFe_2}$ (kJ/mol)	$k_p^{Total} \times 10^{16}$ (m^2/s)	$Q_{k_p}^{Total}$ (kJ/mol)
U vs. Fe	580	12.46 ± 0.49	129.2 ± 10.0	0.36 ± 0.03	224.9 ± 22.3	13.84 ± 0.57	136.9 ± 9.2
	615	28.44 ± 0.65		2.08 ± 0.30		33.51 ± 1.07	
	650	59.44 ± 4.73		8.80 ± 1.41		74.80 ± 6.59	
	680	88.93 ± 4.60		10.21 ± 0.74		109.00 ± 5.85	
	700	117.97 ± 5.55		21.18 ± 1.79		151.70 ± 7.80	
U vs. Fe-15wt.%Cr	600	9.36 ± 0.32	219.7 ± 7.0	0.74 ± 0.09	322.3 ± 34.2	11.11 ± 0.46	230.8 ± 44.7
	650	38.66 ± 1.66		5.34 ± 0.51		48.28 ± 2.34	
	700	210.18 ± 4.91		71.15 ± 9.96		294.64 ± 12.10	
U vs. Fe-15wt.%Cr-15wt.%Ni	600	17.00 ± 0.51	127.3 ± 9.1	0.83 ± 0.14	216.5 ± 22.4	19.45 ± 0.75	135.2 ± 12.3
	650	46.10 ± 2.15		4.49 ± 1.01		55.65 ± 3.47	
	700	103.13 ± 3.45		17.73 ± 2.66		131.95 ± 6.15	

[11]. The thickness of each phase was uniform and the interfaces between phases are planar. Negligible solubility ranges, and thus negligible concentration gradients, are observed within each of the phases. The average thickness, δx^{Phase}, and its standard deviation for the U_6Fe and UFe_2 layers at each temperature were determined [10] as reported in Table 2. The U_6Fe phase is much thicker than UFe_2 in all diffusion couples, although the difference, evaluated by thickness ratio, gets smaller with increasing temperature. Ogata [5] and Nakamura [6] demonstrated that the growth process between U–Zr and Fe are diffusion controlled. Therefore, under the assumption of parabolic growth for both U_6Fe and UFe_2, growth constants for each phase and total interaction zone (i.e., $U_6Fe + UFe_2$) were calculated based on thickness measurement. They are presented in Table 3 along with the standard deviation and in Fig. 3. The temperature dependence of growth for the U_6Fe clearly followed the Arrhenius relation as presented in Fig. 3(a), but that for the UFe_2 exhibited some scatter as shown in Fig. 3(b). The activation energy of growth for each phase was also determined as reported in Table 3 along with the standard deviation.

3.2. U vs. Fe–15 wt.%Cr diffusion couples

Fig. 4 presents the typical BSE micrograph and concentration profiles observed in U vs. Fe–15 wt.%Cr diffusion couple annealed at 650 °C for 96 h. Similar phase constituents, microstructures and concentration profiles were obtained for the U vs. Fe–15 wt.%Cr couples annealed at 600 and 700 °C. The four phases observed in the U vs. Fe–15 wt.%Cr couples were U, U_6Fe, UFe_2 with a significant Cr solubility, and bcc Fe(Cr). Concentration profiles obtained via SEM–XEDS semi-quantitative standard-less analysis shows that there exist a Cr solubility of 12–20 at.% in the UFe_2 (*cF24*, $Fd\bar{3}m$) phase, denoted as $U(Fe,Cr)_2$, while there is negligible solubility of Cr in the U_6Fe (*tI28*, *I4/mcm*). This is consistent with results reported by Nakamura et al. [6]. In the $U(Fe,Cr)_2$, the ratio of (Fe + Cr) to U remains relatively constant at about 2. Information on typical composition determined by SEM–XEDS for the U_6Fe and $U(Fe,Cr)_2$ phases are reported in Table 4.

A Cr enrichment was found near the $U(Fe,Cr)_2$ at the interface between the Fe(Cr) terminal alloy and $U(Fe,Cr)_2$ phase, as well as that between the $U(Fe,Cr)_2$ and U_6Fe phases as shown by the Cr concentration profile in Fig. 4 and XEDS mapping in Fig. 5. The Cr enrichment $U(Fe, Cr)_2$ at the Fe-alloy interface was also observed in investigations reported by Nakamura in U–Zr vs. Fe–Cr [6] couples and by Keiser in U–Zr vs. Fe–Cr–Ni [4] couples. Fig. 4 also shows that Cr appears to interdiffuse uphill against its own gradient but down an Fe concentration gradient within the $U(Fe, Cr)_2$ phase. Consistent observations of Cr enrichment by Nakamura [6], Keiser [4] and this study at either ends of the $U(Fe,Cr)_2$ phase,

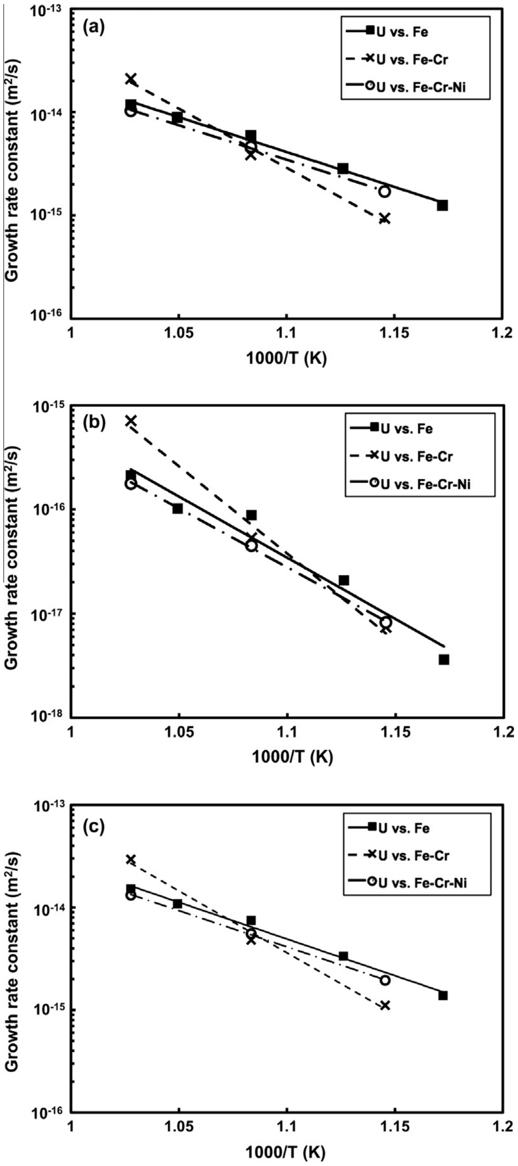

Fig. 3. Temperature dependence of growth rate constants for (a) U_6Fe phase, (b) UFe_2 phase and (c) total interdiffusion zone determined from the diffusion couples, U vs. Fe, U vs. Fe–15 wt.%Cr and U vs. Fe–15 wt.%Cr–15 wt.%Ni. Standard deviations determined for the growth rate constants are reported individually in Table 3.

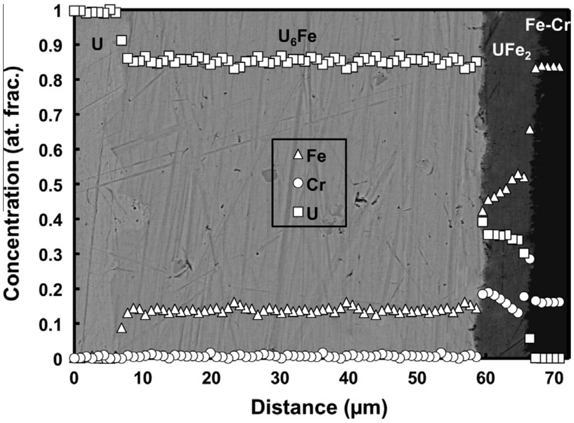

Fig. 4. Backscattered electron micrograph and concentration profiles obtained from the U vs. Fe–15 wt.%Cr diffusion couple annealed at 650 °C for 96 h.

along with evidence of Cr uphill interdiffusion within the $U(Fe,Cr)_2$ phase, warrant a more comprehensive ternary inter-, intrinsic diffusion and phase equilibrium investigations, with emphasis on the relative intrinsic diffusion of Fe and Cr, and changes of solubility in U_6Fe and $U(Fe,Cr)_2$ phases.

The thickness, diffusion-controlled growth rate constant, and activation energy of U_6Fe phase, $U(Fe,Cr)_2$ phase, and the total interaction zone, i.e., $U_6Fe + U(Fe,Cr)_2$, were calculated as reported in Tables 2 and 3. The temperature dependence of growth rates is presented in Fig. 3. Table 2 also shows that the thickness ratios of U_6Fe to $U(Fe,Cr)_2$ are similar in magnitude to those found for U vs. Fe diffusion couples. These ratios decrease with an increase in the temperature of anneal. As shown in Fig. 3 and reported in Table 3, the growth of the U_6Fe phase and the $U(Fe,Cr)_2$ phase in U vs. Fe–15 wt.%Cr diffusion couples exhibits higher activation energies than the growth of U_6Fe and UFe_2 phases in U vs. Fe diffusion couples. It will also be shown in Section 3.3 that these activation energies are higher than those observed for U vs. Fe–Cr–Ni diffusion couples. This is consistent with the higher growth rate at high temperature (e.g., 700 °C), but lower at low temperature, as reported in Tables 2 and 3 for the U vs. Fe–15 wt.%Cr diffusion couples. Hence, the Cr content in the Fe-cladding alloy plays an important temperature-sensitive role for the rate of interdiffusion and reaction.

3.3. U vs. Fe–15 wt.%Cr–15 wt.%Ni diffusion couples

Typical BSE micrograph and concentration profiles obtained from the U vs. Fe–15 wt.%Cr–15 wt.%Ni diffusion couple annealed at 700 °C for 96 h are presented in Fig. 6. SEM-XEDS element mapping from this couple is presented in Fig. 7. Similar microstructures, concentration profiles and elemental maps were obtained from the couples annealed at 600 and 650 °C. A distinctive feature observed in the U vs. Fe–15 wt.%Cr–15 wt.%Ni diffusion couple is the presence of a two-phase (i.e., UFe_2 and Fe–Cr–Ni solid solution) layer between the Fe–15 wt.%Cr–15 wt.%Ni terminal alloy, and the UFe_2 phase with clear solubility for both Ni (14 at.%) and Cr (3–7 at.%).

The main four phases observed in the U vs. Fe–15 wt.%Cr–15 wt.%Ni couples were U, U_6Fe (*tI28*, *I4*/*mcm*) with some solubility for Ni (2.5 at.%), denoted as $U_6(Fe,Ni)$, UFe_2 (*cF24*, $Fd\bar{3}m$) with solubilities for both Ni and Cr, denoted as $U(Fe,Ni,Cr)_2$, and fcc Fe(Ni,Cr) as presented in Fig. 6. The composition of the U_6Fe phase remained relatively constant throughout the thickness, approximately at

Table 4
Composition of U_6Fe and UFe_2 phases in the U vs. Fe–15 wt.%Cr and U vs. Fe–15 wt.%Cr–15 wt.%Ni diffusion couples.

Diffusion couples	Composition of U_6Fe (at.%)				Composition of UFe_2 (at.%)			
	U	Fe	Cr	Ni	U	Fe	Cr	Ni
U vs. Fe–15 wt.%Cr	85	15	Negligible	N.A.	35	45–53	12–20	N.A.
U vs. Fe–15 wt.%Cr–15 wt.%Ni	85	12.5	Negligible	2.5	35	44–48	3–7	14

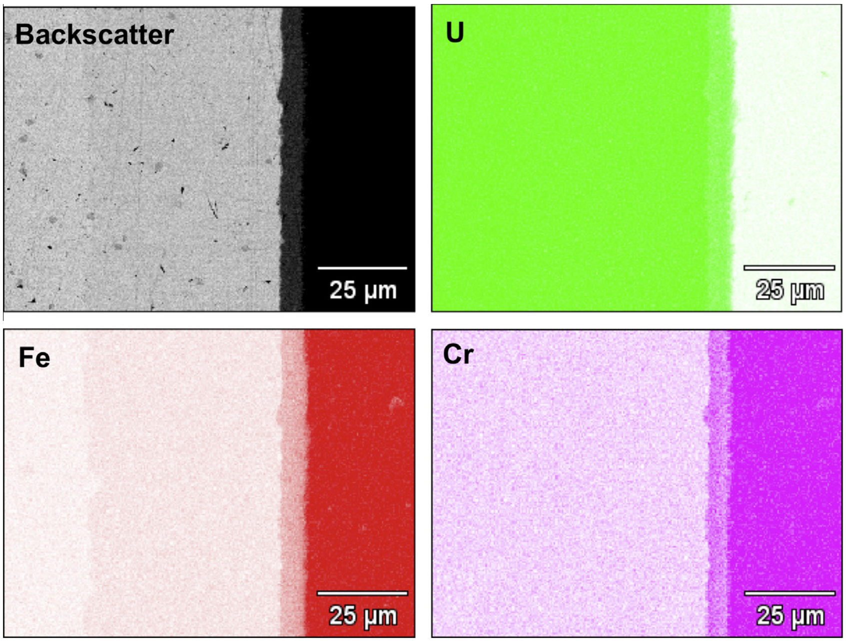

Fig. 5. X-ray energy dispersive elemental mapping obtained from the U vs. Fe–15 wt.%Cr diffusion couple annealed at 650 °C for 96 h.

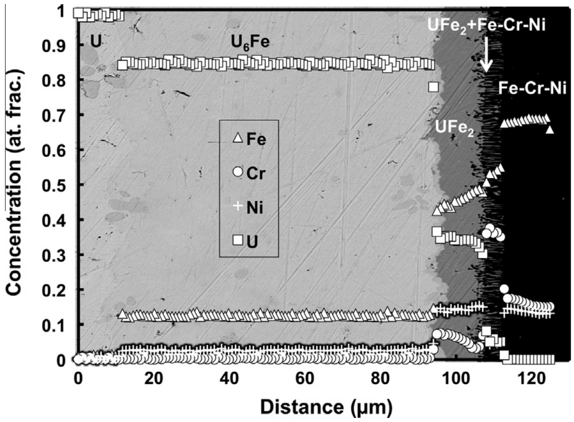

Fig. 6. Backscattered electron micrograph and concentration profiles obtained from the U vs. Fe–15 wt.%Cr–15 wt.%Ni diffusion couple annealed at 700 °C for 96 h.

85 at.% U, 12.5 at.% Fe, 2.5 at.% Ni with negligible Cr content. Solubility of Ni in U_6Fe phase is consistent with presence of U_6Ni in the binary phase diagram of U–Ni system [11]. The concentrations of Fe, Cr, Ni and U in $U(Fe,Ni,Cr)_2$ were 44–48, 3–7, 14, and 35 at.%, respectively, and the concentration ratio of (Fe + Cr + Ni) to U remained at approximately 2 despite the presence of concentration gradient. Information on typical compositions of the $U_6(Fe,Ni)$ and $U(Fe,Ni,Cr)_2$ are reported in Table 4. A few darker gray inclusions were observed randomly on the pure terminal U alloy, and they were identified as carbides of uranium based on XEDS semi-quantitative composition analysis.

Concentration profiles in Fig. 6 and XEDS element maps in Fig. 7 shows that U vs. Fe–15 wt.%Cr–15 wt.%Ni diffusion couples also developed Cr-enriched regions: the two phase regions between the $U(Fe,Ni,Cr)_2$ and Fe–Cr–Ni terminal solid solution; and within the $U(Fe,Ni,Cr)_2$ layer near the interface between the $U_6(Fe,Ni)$ and $U(Fe,Ni,Cr)_2$ layers. These Cr-enrichment locations are similar to those observed in U vs. Fe–15 wt.%Cr diffusion couples, and may be explained by rapid intrinsic diffusion and larger solubility of Fe and Ni in both $U(Fe,Ni,Cr)_2$ and $U_6(Fe,Ni)$ phases.

The thickness, parabolic growth rate constants and their activation energies for the $U_6(Fe,Ni)$, $U(Fe,Ni,Cr)_2$, and total summation of the interaction zone are reported in Tables 2 and 3. Fig. 3 shows the temperature dependence of the parabolic growth rate constants. The temperature dependence and activation energy for the growth of $U_6(Fe,Ni)$ and $U(Fe,Ni,Cr)_2$ are similar to those determined for U_6Fe and UFe_2 from the U vs. Fe binary diffusion couples. However, the magnitude of the growth constants is slightly smaller for $U_6(Fe,Ni)$ and $U(Fe,Ni,Cr)_2$ than the respective binary U_6Fe and UFe_2.

4. Cumulative interdiffusion fluxes

To examine and compare the interdiffusion behavior quantitatively, integrated interdiffusion coefficients that reflect the cumulative interdiffusion fluxes of individual components were determined from the diffusion couples. Since these coefficients do not require accurate assessment of concentration gradient, concentration profiles obtained from semi-quantitative, standard-less

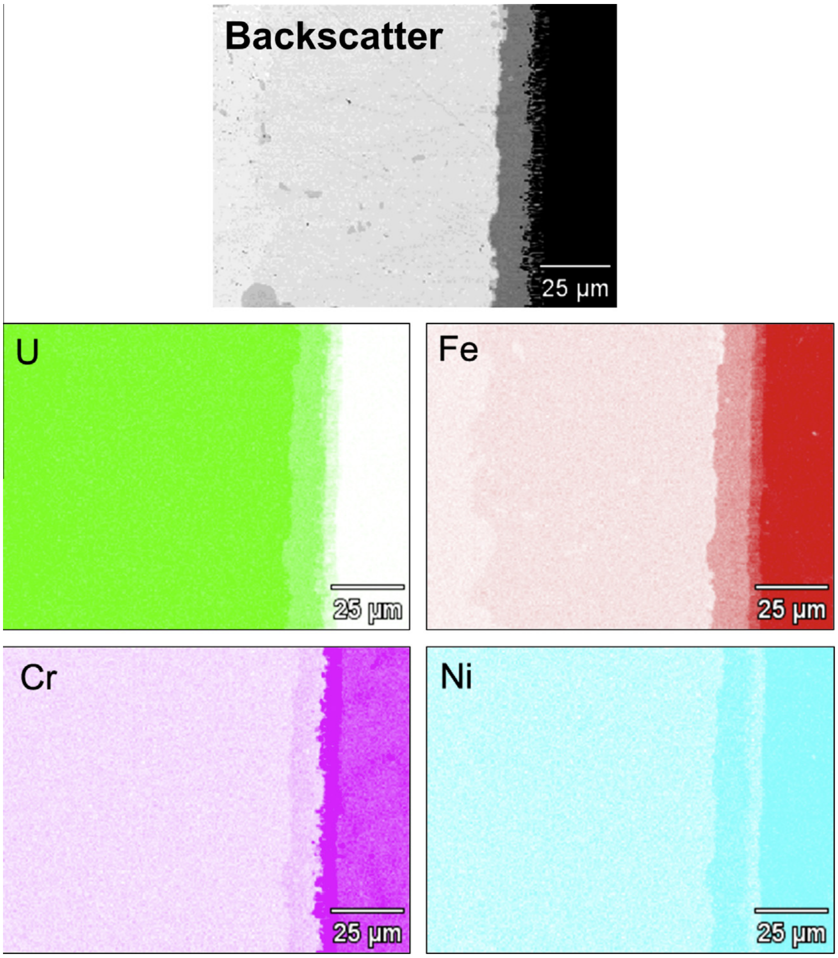

Fig. 7. X-ray energy dispersive elemental mapping obtained from the U vs. Fe–15 wt.%Cr–15 wt.%Ni diffusion couple annealed at 650 °C for 96 h.

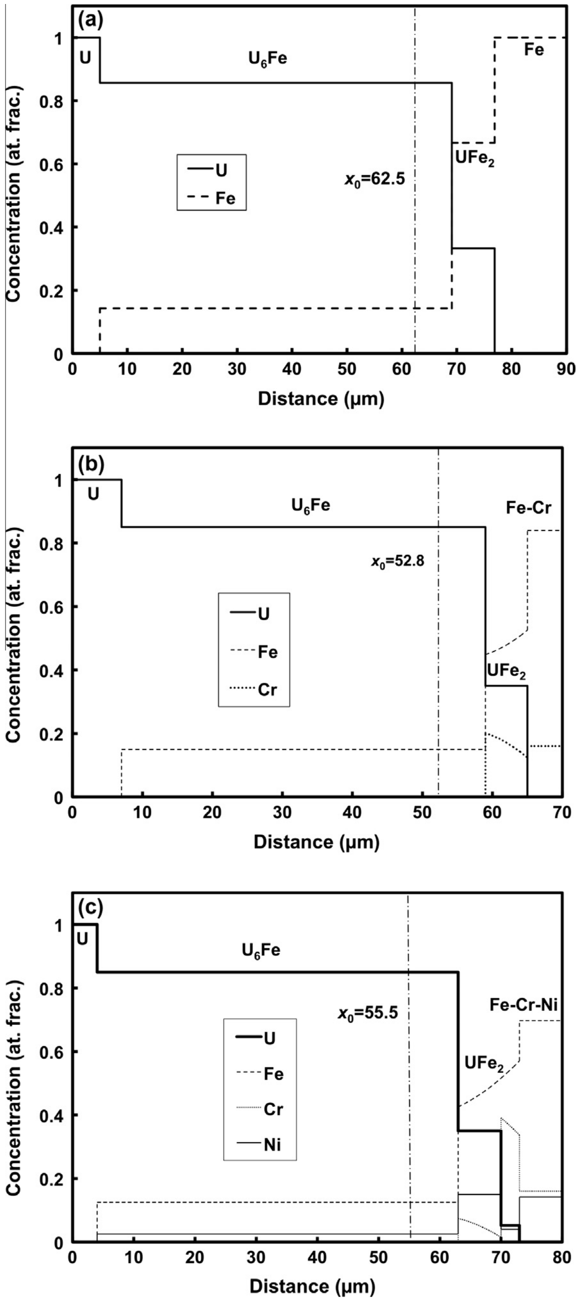

Fig. 8. Smoothened concentration profiles of (a) U vs. Fe, (b) U vs. Fe–15 wt.%Cr and (c) U vs. Fe–15 wt.%Cr–15 wt.%Ni diffusion couples annealed at 650 °C for 96 h.

XEDS were first simplified and smoothened as presented in Fig. 8. Following the procedure proposed by Dayananda [12], interdiffusion fluxes for individual components were computed by:

$$\tilde{J}_i = \frac{1}{2t}\int_{C_i^{-\infty}}^{C_i^{*}} (x - x_o)\; dC_i \quad (i = \mathrm{U, Fe, Cr\ or\ Ni}) \tag{1}$$

where C_i^* is the concentration of component i at which the interdiffusion flux is determined, and t refers to the time of diffusion anneal, and x_o is the Matano plane. For each relevant phase observed in this study, the cumulative interdiffusion fluxes of individual components were calculated as the integrated interdiffusion coefficient given by:

$$\tilde{D}_i^{\mathrm{Int,Phase}} = \int_{x_i^1}^{x_i^2} \tilde{J}_i(x)dx \quad (i = \mathrm{U, Fe, Cr\ or\ Ni}) \tag{2}$$

where x_i^1 and x_i^2 correspond to the location of interphase boundaries. It should be noted that the magnitude of $\tilde{D}_i^{\mathrm{Int,Phase}}$'s corresponds to the cumulative interdiffusion fluxes of individual components within a phase based on the reference frame of Matano plane, and must not be interpreted as the interdiffusion coefficients. The uncertainty in $\tilde{D}_i^{\mathrm{Int,Phase}}$'s calculated in this study mostly arise from the variation in measured thickness of individual phases, and can vary within 10% in magnitude (see for example standard deviation reported for growth constant in Table 3). The average effective interdiffusion coefficients, $\tilde{D}_i^{\mathrm{eff}}$, in a phase can be determined, given a sufficient solubility range ΔC_i, by:

$$\tilde{D}_i^{\mathrm{eff}} = \frac{\int_{x_i^1}^{x_i^2} \tilde{J}_i(x)dx}{\Delta C_i} \quad (i = \mathrm{U, Fe, Cr\ or\ Ni}) \tag{3}$$

Unfortunately, in this study a sufficient solubility range ΔC_i for a given phase for all individual components could not be determined consistently and, thus, $\tilde{D}_i^{\mathrm{eff}}$'s were not evaluated.

Table 5 reports that the magnitude of calculated $\tilde{D}_i^{\mathrm{Int,Phase}}$'s for the U$_6$Fe phase is higher in general than that for the UFe$_2$ phase, consistent with the faster growth of U$_6$Fe phase. In both intermetallic phases, U and Fe have higher $\tilde{D}_i^{\mathrm{Int,Phase}}$'s than Cr or Ni, mainly from the larger concentration differences imposed by the terminal alloy compositions. However, the temperature dependence of $\tilde{D}_i^{\mathrm{Int,Phase}}$'s, represented by the activation energies, $\tilde{Q}_i^{\mathrm{Int,Phase}}$'s, show that Cr has a higher activation energy and strong influence for the temperature-dependent interdiffusion process in UFe$_2$ phase, particularly considering the U vs. Fe–15 wt.%Cr without the Ni addition. Similar observation of Cr effect can be observed in Table 3 for U vs. Fe–15 wt.%Cr without the Ni addition. While the same can said for the interdiffusion of Ni in UFe$_2$ phase, the magnitudes of $\tilde{Q}_{\mathrm{Ni}}^{\mathrm{Int,U_6Fe}}$ and $\tilde{Q}_{\mathrm{Ni}}^{\mathrm{Int,Total}}$ are similar to those of U and Fe, because U$_6$Fe (with negligible solubility for Cr) is the thicker, faster-growing phase in all diffusion couples. This temperature sensitivity of Cr addition is consistent with the temperature-dependence of growth constants determined from U vs. Fe–Cr diffusion couples.

5. Summary

In this study, the interdiffusion and reaction between U and Fe, Fe–Cr or Fe–Cr–Ni alloy were examined. The intermetallic phases that developed in diffusion couples U vs. Fe were U$_6$Fe (*tI28*, *I4/mcm*) and UFe$_2$ (*cF24*, *Fd*$\bar{3}$*m*) phases. With addition of Cr in bcc Fe–Cr alloy, the solubility of Cr up to 20 at.% was observed in the UFe$_2$ phase, while the U$_6$Fe phase did not exhibit any solubility for Cr. With the addition of both Ni and Cr in the fcc Fe–Cr–Ni alloy, a small solubility up to 2.5 at.% for Ni was found in the U$_6$Fe phase, while both Cr and Ni were found to be dissolved in the UFe$_2$ phase, up to 7 at.% and 14 at.%, respectively. These observations of phase constituents and compositions agree with the previous studies on reactions between U–Zr and Fe–Cr–Ni alloys [4,6], and In all diffusion couples, the U$_6$Fe phase was observed to grow much thicker than the UFe$_2$ phase, regardless of changes in solubilities.

The growth rate constants of U$_6$Fe, UFe$_2$ and total interdiffusion zone in the three types of diffusion couples were calculated under the assumption of parabolic growth. The interdiffusion and reactions in the U vs. Fe and U vs. Fe–Cr–Ni show similar temperature dependence, while the U vs. Fe–Cr diffusion couples exhibited a larger magnitude of activation energy for growth constants and integrated interdiffusion coefficients for Cr. The effect of the Cr addition was further quantified with the determination of integrated interdiffusion coefficients. The integrated interdiffusion of Cr in the U(Fe,Cr)$_2$ had a larger magnitude of activation energy and was primarily responsible for the higher temperature sensitivity of interdiffusion and reaction observed in U vs. Fe–Cr diffusion couples.

Table 5
Cumulative interdiffusion fluxes of individual components numerated by the magnitude of integrated interdiffusion coefficients determined for the U_6Fe, UFe_2 and total interdiffusion zone from the U vs. Fe [10], U vs. Fe–15 wt.%Cr and U vs. Fe–15 wt.%Cr–15 wt.%Ni diffusion couples. Note that with the alloying addition of Cr and Cr–Ni in Fe–15 wt.%Cr and Fe–15 wt.%Cr–15 wt.%Ni alloys, respectively, results in the formation of UFe_2 and U_6Fe with variation in solubilities for Cr and Ni.

Diffusion couple	*i*	*T* (°C)	$\tilde{D}_i^{Int,U_6Fe} \times 10^{16}$ (atf-m^2/s)	$\tilde{Q}_i^{Int,U_6Fe}$ (KJ/mole)	$\tilde{D}_i^{Int,UFe_2} \times 10^{17}$ (atf-m^2/s)	$\tilde{Q}_i^{Int,UFe_2}$ (KJ/mole)	$\tilde{D}_i^{Int,Total} \times 10^{16}$ (atf-m^2/s)	$\tilde{Q}_i^{Int,Total}$ (KJ/mole)
U vs. Fe	U or Fe	580	1.56	130.89	0.40	190.83	1.60	133.59
		615	3.60		1.62		3.76	
		650	7.63		5.40		8.17	
		680	11.35		6.80		12.03	
		700	15.21		12.2		16.43	
U vs. Fe–15 wt.%Cr	U	600	1.63	145.15	1.16	161.57	1.75	146.37
		650	5.33		4.15		5.74	
		700	12.71		11.39		13.85	
	Fe	600	1.61	145.17	1.37	153.98	1.75	145.90
		650	5.21		4.52		5.70	
		700	12.54		12.15		13.75	
	Cr	600	No observable solubility was found		0.01	190.27	0.01	190.27
		650			0.04		0.04	
		700			0.12		0.12	
U vs. Fe–15 wt.%Cr–15 wt.%Ni	U	600	2.58	99.23	1.78	116.20	2.76	100.46
		650	6.86		5.31		7.39	
		700	10.42		9.17		11.33	
	Fe	600	2.08	99.63	1.38	115.43	2.22	100.72
		650	5.58		4.30		6.01	
		700	8.46		7.00		9.16	
	Cr	600	No observable solubility was found		0.03	164.78	0.03	164.78
		650			0.15		0.15	
		700			0.28		0.28	
	Ni	600	0.41	98.53	0.02	217.54	0.41	100.04
		650	1.09		0.21		1.12	
		700	1.65		0.44		1.69	

6. US department of energy disclaimer

This information was prepared as an account of work sponsored by an agency of the US Government. Neither the US Government nor any agency thereof, nor any of their employees, makes any warranty, express or implied, or assumes any legal liability or responsibility for the accuracy, completeness, or usefulness of any information, apparatus, product, or process disclosed, or represents that its use would not infringe privately owned rights. References herein to any specific commercial product, process, or service by trade name, trademark, manufacturer, or otherwise, does not necessarily constitute or imply its endorsement, recommendation, or favoring by the US Government or any agency thereof. The views and opinions of authors expressed herein do not necessarily state or reflect those of the US Government or any agency thereof.

Acknowledgements

This work was supported by the US Department of Energy under DOE-NE Idaho Operations Office Contract DE-AC07-05ID14517. Accordingly, The US Government retains and the publisher, by accepting the article for publication, acknowledges that the US Government retains a nonexclusive, paid-up, irrevocable, world-wide license to publish or reproduce the published form of this manuscript, or allow others to do so, for US Government purposes.

References

[1] G.L. Hofman, L.C. Walters, T.H. Bauer, Prog. Nucl. Energy 31 (1997) 83.
[2] W.J. Carmack, D.L. Porter, Y.I. Chang, S.L. Hayes, M.K. Meyer, D.E. Burkes, C.B. Lee, T. Mizuno, F. Delage, J. Somers, J. Nucl. Mater. 392 (2009) 139.
[3] D. Olander, J. Nucl. Mater. 389 (2009) 1.
[4] D.D. Keiser Jr, M.A. Dayananda, J. Nucl. Mater. 200 (1993) 229.
[5] T. Ogata, M. Kurata, K. Nakamura, A. Itoh, M. Akabori, J. Nucl. Mater. 250 (1997) 171.
[6] K. Nakamura, T. Ogata, M. Kurata, A. Itoh, M. Akabori, J. Nucl. Mater. 275 (1999) 246.
[7] G.L. Hofman, A.G. Hins, D.L. Porter, L. Leibowitz, E.L. Wood, Chemical interaction of metallic fuel with austenitic and ferritic stainless steel cladding, International conference on reliable fuels for liquid metal reactors. Tucson, Arizona, 1986.
[8] D. Keiser, M. Dayananda, Metall. Mater. Trans. A 25 (1994) 1649.
[9] C.T. Lee, H. Kim, T.K. Kim, C.B. Lee, J. Nucl. Mater. 395 (2009) 140.
[10] K. Huang, Y. Park, A. Ewh, B.H. Sencer, J.R. Kennedy, K.R. Coffey, Y.H. Sohn, J. Nucl. Mater. 424 (2012) 82.
[11] T.B. Massalski (Ed.), Binary Phase Diagrams, second ed., American Society for Metals, 1990.
[12] M.A. Dayananda, Metall. Mater. Trans. 14A (1983) 1851.